Design and performance evaluation of a large field-of-view dual-particle time-encoded imager based on a depth-of-interaction detector

Dong Zhao[1], Xu-Wen Liang[1], Ping-Kun Cai[1], Wei Cheng[1], Wen-Bao Jia[1,2,*], Da-Qian Hei[2,3,*],

Qing Shan[1,2], Yong-Sheng Ling[1,2], Chao Shi[1,2]

1 Department of Nuclear Science and Technology, Nanjing University of Aeronautics and Astronautics, Nanjing, 211106, China.

2 Collaborative Innovation Center of Radiation Medicine of Jiangsu Higher Education Institutions, Suzhou, 215000, China.

3 School of Nuclear Science and Technology, Lanzhou University, Lanzhou, 730000, China.

* Corresponding Authors:

Dr. Wen-Bao Jia, E-mail address: jiawb@nuaa.edu.cn, Tel: +86-025-52112626;

Dr. Da-Qian Hei, E-mail address: heidq@lzu.edu.cn, Tel: +86-0931-8913551.

Abstract: Time-encoded imaging is useful for identifying potential special nuclear materials and other radioactive sources at a distance. In this study, a large field-of-view time-encoded imager was developed for gamma-ray and neutron source hotspot imaging based on a depth-of-interaction (DOI) detector. The imager primarily consists of a DOI detector system and a rotary dual-layer cylindrical coded mask. An EJ276 plastic scintillator coupled with two SiPMs was designed as the DOI detector to increase the field of view and improve the imager performance. The difference in signal time at both ends and the log of the signal amplitude ratio were used to calculate the interaction position resolution. The position resolution of the DOI detector was calibrated using a collimated Cs-137 source, and the full width at half maximum of the reconstruction position of the Gaussian fitting curve was approximately 4.4 cm. The DOI detector can be arbitrarily divided into several units to independently reconstruct the source distribution images. The unit length was optimized via Am-Be source-location experiments. A multidetector filtering method is proposed for image denoising. This method can effectively reduce image noise caused by poor DOI detector position resolution. The vertical field of view of the imager was (-55°, 55°) when the detector was placed in the center of the coded mask. A DT neutron source at 20 m standoff could be located within 2400 s with an angular resolution of 3.5°.

Keywords: time-encoded imager; depth-of-interaction detector; dual-particle imaging; hotspot imaging

1 Introduction

Gamma-ray and neutron source hotspot imaging has emerged as a critical tool for monitoring radiation facilities and preventing the illicit transportation of nuclear materials [1, 2]. This imaging technique has significant academic importance in the fields of radiation safety, nuclear security, and non-proliferation. In the realm of radiation facility monitoring, gamma-ray and neutron source

hotspot imaging provides valuable insights into the spatial distribution and intensity of radiation sources within these facilities [3]. Furthermore, it aids in the identification and characterization of localized regions with elevated radiation levels, enabling facility operators to assess potential hazards and effectively mitigate risks [4]. Previous studies have contributed to the development of mathematical models and simulation techniques that provide quantitative analyses and predictive capabilities for radiation distribution within facilities. From a nuclear security perspective, gamma-ray and neutron source hotspot imaging plays a vital role in countering the illicit transportation of nuclear materials. Academic research has focused on the development of sophisticated detectors and imaging systems capable of detecting shielded or hidden radioactive sources. These previous studies [2–5] investigated various detection principles such as gamma-ray spectroscopy, neutron counting [6], and imaging algorithms [7] to enhance the sensitivity, resolution, and efficiency of hotspot imaging. Furthermore, researchers [8, 9] have analyzed the use of advanced data analysis techniques, including machine learning and artificial intelligence, to improve the detection and classification of potential threats in a real-time basis. Contributions in this regard have helped develop robust methodologies and protocols for the reliable identification of illicit nuclear materials during transportation [10], thus strengthening international nuclear security. Additionally, advanced imaging algorithms [12] and processing techniques [13] have been explored to extract valuable information from hotspot images, enabling a more accurate and reliable radiation source location identification. Furthermore, academic research has been conducted to assess the challenges and limitations associated with gamma-ray and neutron source hotspot imaging. These studies [10–13] aim to refine imaging techniques, enhance radiation detection sensitivity, and reduce false-alarm rates. Contributions from the academic community have facilitated the development of standardized procedures, calibration methodologies, and performance evaluation criteria for hotspot imaging systems to ensure consistent and reliable results across different applications and environments.

The three commonly used instruments for dual-particle (gamma ray and neutron) hotspot imaging are neutron-scattering (Compton) cameras, spatially coded aperture imagers, and time-encoded imagers. A neutron-scattering camera typically consists of a two-layer organic scintillator detector array [14]. The incident neutron (photon) interacts with the first-layer detector, which records the energy of the recoil proton (electron). Scattered neutrons (photons) can be detected by the next-layer detector. The time-of-flight between the two detectors is used for neutron/gamma-ray discrimination and to calculate the energy of the scattered neutrons. Because the time-of-flight method is used for neutron/gamma-ray discrimination, individual detectors do not require such discrimination capabilities. The energy of the recoil protons and scattered neutrons can be used to calculate the incident direction relative to the detector position [15,16]. These coincidence events are used to determine the position of the radioactive sources. The sensitivity (efficiency) of scattering cameras is low because of the requirement of coincidence events. In some scattering camera designs, an additional inorganic scintillator array layer is added to improve the gamma-ray detection efficiency. Some compacted designs based on a depth-of-interaction (DOI) detector is proposed for obtaining a 4π field-of-view (FOV); however, the FOV is non-uniform and the sensitivity further reduces due to the small detector size [17]. A spatially coded aperture imager typically consists of a detector array and a stationary coded mask [18, 19]. The detector should enable neutron/gamma-ray discrimination [20], and the coded mask should shield fast neutrons and gamma rays for dual-particle measurements. Similar to the gamma-ray camera principle, the

count pattern of the detector array differs because of the presence of a coded mask [21]. The radioactive source can be located based on the count pattern of the detector array. In addition, spatially coded aperture imagers exhibit an excellent angular resolution and sensitivity. However, the relative position between the detector array and coded mask limits the FOV in certain directions [22, 23]. In a time-encoded imager, the device typically consists of a single detector and a moving coded mask [24, 25]. A rotating cylindrical coded mask around the detector is the most commonly used mask design for increasing the FOV [26–29]. If there is a radioactive source in the imager FOV during a measurement, the count rate changes over the rotation angle as the cylindrical mask rotates around the detector. In other words, the count rate of the detector changes over time. Therefore, the device is called a time-encoded imager. The count vector varies when the source is at a different position.

As mentioned above, compared with neutron-scattering cameras and spatially coded aperture imagers, the most important feature of time-encoded imagers is that they require only one detector rather than a detector array. Therefore, they offer advantages such as lower cost, fewer detectors, lower device complexity, high detection efficiency, and a large FOV [29, 30]. In previous studies, one- and two-dimensional time-encoded imagers with different coded masks and central detectors were designed for neutron and gamma-ray source hotspot imaging [31–33]. The detection efficiency (sensitivity) and angular resolution are the two most important performance metrics for time-encoded imagers [34]. The central detector and coded mask are key components that affect the imager performance [35, 36]. For the central detector, the larger the volume of the detector, the higher the detection efficiency of the imager but the worse the angular resolution. In other words, time-encoded imagers have a trade-off between detection efficiency and angular resolution caused by the detector size. To improve the detection efficiency, the length of the detector must be increased; while to maintain a high angular resolution and low device complexity, a dual-ended readout DOI detector design is adopted to determine the particle interaction position.

In this study, a large FOV dual-particle time-encoded imager based on a DOI detector was designed for performance optimization. The DOI detector based on a dual-ended readout EJ276 plastic scintillator was calibrated for position resolution. An image-denoising method for DOI detector-based time-encoded imaging is proposed to suppress random noise in the reconstructed source distribution. The performance of this imager, including its FOV and sensitivity, was evaluated experimentally.

2 Materials and Methods

The dual-particle time-encoded imager primarily consists of a DOI detector (central detector) and a rotating dual-layer cylindrical coded mask. The detector is placed at the center of the mask. This section describes the design of the central detector, coded mask, and image reconstruction method.

2.1 Depth-of-interaction detector configuration and position response principle

A DOI detector is a type of radiation detector designed to determine the depth or position at which a radiation event occurs within the detector volume. Traditional radiation detectors, such as scintillation detectors, provide energy information but not accurate positional information for radiation events that occur within the detector. DOI detectors are particularly important in applications that require accurate spatial resolution, such as medical imaging [37], high-energy physics experiments, and nuclear imaging. Image quality can be improved by providing a more

precise radiation event localization, leading to better resolution, reduced blurring, and increased sensitivity.

Several techniques have been used to measure the DOI in detectors. One common approach is to use scintillation crystals with unique light output distributions along the crystal depth [38]. The scintillation light is read out by an array of photodetectors, and the variation in the light distribution allows the determination of the interaction depth. This technique is commonly used in positron emission tomography (PET) scanners, where DOI detectors can improve the spatial resolution and image quality [39]. Another approach is to use pixelated or segmented detectors, in which each segment or pixel has its own readout electronics. By analyzing the signals from different segments, the DOI detector can determine the interaction depth based on the energy deposition distribution within the detector. In a dual-particle time-encoded imager, neutron/gamma-ray discrimination capability is a basic requirement for the central detector. The central detector should preferably have high detection efficiencies for fast neutrons and gamma rays. Plastic (EJ276), liquid, and CLYC scintillators are candidates for the central detector. These scintillators have good neutron/gamma-ray discrimination capabilities. A CLYC scintillator is difficult to machine to such lengths (more than 10 cm) and is relatively expensive. Furthermore, its intrinsic detection efficiency for fast neutrons is relatively low, approximately 1%, which is significantly lower than that of organic scintillators. When comparing plastic and liquid scintillators, the primary concern revolves around the processing challenges. In this study, a one-dimensional position-sensitive detector based on a dual-ended readout rod-shaped EJ276 plastic scintillator [40] was designed and assembled. The design and position response principle of the detector is described next.

As shown in Figure 1(a), the EJ276 plastic scintillator (size: Φ3 cm × 15 cm) coupled with two SiPMs (SensL, ARRAYJ-60035-4P) was encapsulated in an aluminum housing. The diameter and length of the detector were 3.5 and 21 cm, respectively. The reflector between the aluminum shell and scintillator consists of a 0.12-mm layer of white nylon and a 50-μm aluminized film. The white nylon serves as a reflective medium, helping to enhance the reflection of light towards the scintillator, while the aluminized film provides additional reflection and helps minimize light loss. This combination of materials effectively optimizes the light collection efficiency of the detector system. The active area of the SiPM (2×2) was 12.46 × 12.46 mm^2. The two SiPMs were powered using a voltage power supply (RIGOL DP832). The operating voltage of the SiPM was set to +29.5 V (available voltage range: +24–30 V). The output signals were recorded using a Desktop Waveform Digitizer (CAEN, DT5730). The amplitude, incident time, and pulse shape discrimination (PSD) of each signal were recorded for pulse shape discrimination and position resolution.
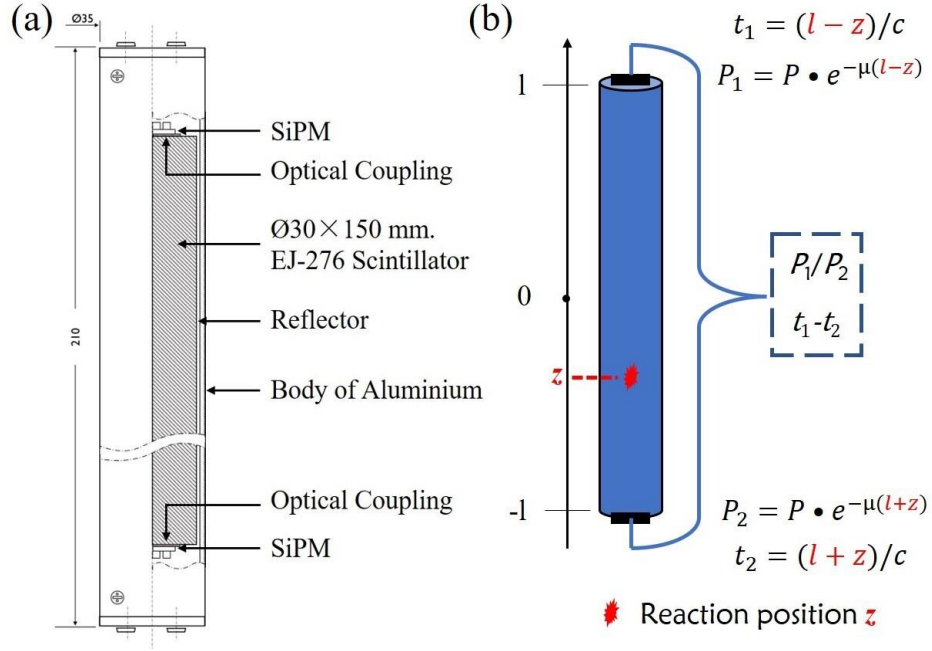
4

Figure 1. (a) Structure of the DOI detector; (b) position resolution principle.

In general, when a particle interacts with a scintillator, the signal is recorded at both ends at short intervals. The difference between the signals at the two ends is used to determine the interaction position. The difference in time and log of the signal amplitude ratio can be used for position resolution. As shown in Figure 1(b), the length of the scintillator is $2l$; the coordinate origin is the center of the detector; the interaction location, i.e., the coordinates of the scintillation light production location, is z; the number of scintillation photons produced in an interaction is $2P$; the linear attenuation coefficient of the scintillator is μ; and the photon transport speed in the scintillator is c.

The number of photons arriving at each end of the detector is as follows:

$$P_1 = P \bullet e^{-\mu(l-z)} \qquad\qquad Eq.\,1$$
$$P_2 = P \bullet e^{-\mu(l+z)} \qquad\qquad Eq.\,2$$

The signal amplitudes A_1, A_2 are proportional to P_1, P_2, respectively. Theoretically, the interaction location z can be determined based on the log of the signal amplitude ratio, as follows:

$$z = \frac{1}{2\mu}\ln\frac{A_1}{A_2} \qquad\qquad Eq.\,3$$

The moment when the signal arrives at each end of the detector is given by

$$t_1 = (l-z)/c \qquad\qquad Eq.\,4$$
$$t_2 = (l+z)/c \qquad\qquad Eq.\,5$$

Then, z can be determined based on the difference in times as

$$z = \frac{c \bullet (t_2 - t_1)}{2} \qquad\qquad Eq.\,6$$

In the above theoretical derivation, the diameters of the detector and uncollected photons were ignored, and the reflector reflectivity was treated as 100%. Therefore, z cannot be directly calculated using Eqs. 3 and 6. The relationship between z and the difference in times/log of the signal amplitude ratio must be determined through calibration experiments.

2.2 Cylindrical coded mask design

An image of the time-encoded imager is shown in Figure 2(a). The coded mask design principle and configuration have been introduced in a previous study [29].
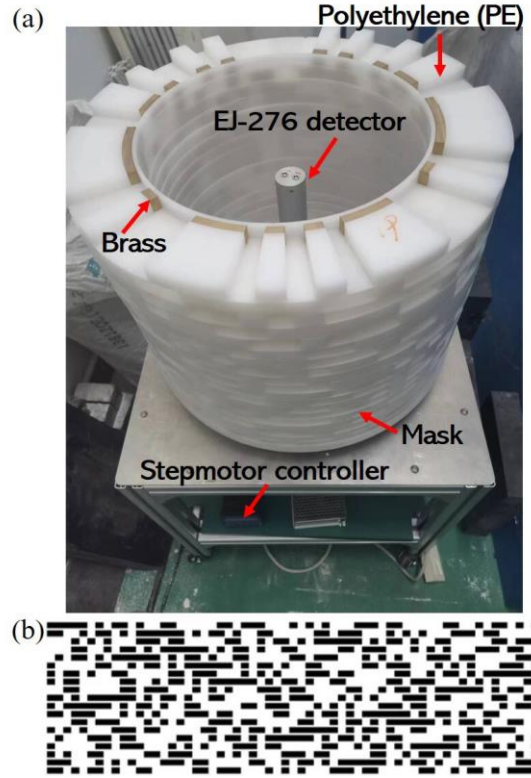

Figure 2 (a) Image of the time-encoded imager; (b) mask pattern of the coded mask.

The materials used for the outer and inner masks were polyethylene (PE) and brass, respectively. Polyethylene with a 6-cm thickness was used to modulate the fast neutrons. Brass with a 0.9-cm thickness was used to modulate the gamma rays. The mask patterns for fast neutrons and gamma rays were identical, as shown in Figure 2(b). The height of each layer was 1.63 cm, and the height of the aperture was reduced to 1.43 cm for easier processing. The center of the detector was positioned approximately 70 cm above the ground. During the measurement process, a coded mask was employed, which was rotated at a uniform speed. The rotational speed of the mask was adjusted using a stepmotor controller. For more information on the dimensions of the coded mask, please refer to [41].

The position response function was simulated using MCNP 5. In this simulation, the detector was divided into 15 basic units (1 cm), allowing a detailed analysis of its response characteristics. The response of each unit was recorded using Tally F4. In other words, the position miscue was ignored and the efficiencies of the different units were considered identical. However, the detection efficiencies of different detector units may differ owing to the different coincidence rates at both ends. The position miscue was treated as a count error in the image reconstruction. The neutron (Cf-252) and gamma-ray (Cs-137) sources were located 3 m from the detector. The response function is significantly influenced by the energy and distance of the radioactive source from the detector. However, during actual measurements, the energy and distance of a probable radioactive source are typically unknown. As per geometric calculations, the vertical and horizontal FOV for this time-encoded imager were established as -60°~60° and 0°~360°,

respectively. The smallest angular pixel was set to 1°. Given the properties of the EJ276 detector, the energy threshold of Tally F4 for neutrons and gamma rays were determined to be 0.5 and 0.2 MeV, respectively. The response function of a detector unit of varying lengths can be deduced by adding the responses from the corresponding basic units.

2.3 Image reconstruction and denoising methods

2.3.1 Image reconstruction method

If there is a radioactive source in the imager FOV, the count rate of the central detector changes with the rotation angle (measurement time). The measured count vector (counts at different angles) C during the measurement can be expressed as

$$C = S \odot R + B \qquad\qquad Eq.7$$

where R is the simulated position response function; S is the actual source distribution; and B is the background count vector, which theoretically does not vary with the rotation angle. However, due to statistical fluctuations, the background counts also vary. In image reconstruction, the background count B is considered an error of C. It is worth noting that the neutron background count rate is much lower than that of gamma rays. Of course, the error in the measured count vector C and the preset response function will affect the reconstructed source distribution.

Maximum likelihood expectation maximization (MLEM) is an iterative algorithm commonly used in image reconstruction [42], particularly in medical imaging techniques such as PET, single-photon emission computed tomography (SPECT), and time-encoded imaging. The MLEM method is used to estimate the underlying image from the acquired data by maximizing the likelihood of the observed data, given the image information. The iterative steps of the MLEM algorithm for time-encoded imaging are as follows:

$$S^{k+1}(i,j) = S^k(i,j) \bullet \left[R(i,j) \odot \frac{C(i)}{S^k(i,j) * R(i,j)} \right] \qquad\qquad Eq.8$$

where $S^k(i,j)$ is the probability of pixel (i,j) in the k-th iteration, $R(i,j)$ is the preset response function, $C(i)$ is the measured count at (measurement time bin i) rotation angle i. The MLEM algorithm aims to converge to an image estimate that maximizes the likelihood of producing the acquired data by assuming a statistical model of the imaging system. It incorporates both forward-(simulation) and back-projection (reconstruction) steps, repeatedly refining the estimated image until convergence is achieved. A step-by-step explanation of the MLEM algorithm is as follows.

1. Initialization: The algorithm begins with an initial estimate of the image, which is often a uniform- or low-resolution image. In this study, a uniform image was used as the initial estimate.

2. Forward projection: The estimated image is forward projected to obtain a modeled projection of the image. This step simulates the appearance of the image data if the estimated image is the true image.

3. Scaling: The modeled projection is scaled to match the measured or acquired projection data in terms of counts or intensity.

4. Back projection: The scaled modeled projection is back-projected into the image space, spreading the modeled counts or intensity back to the pixel grid.

5. Expectation: The acquired projection data are compared with the back-projected result. The ratio of the measured to the modeled data is computed for each pixel or voxel, representing the expectation of the underlying counts or intensity.

6. Maximization: The estimated image is updated by multiplying it element-wise by the ratio calculated in the expectation step. This step increases the contribution of image elements that are

more likely to produce the observed data.

7. Repeat Steps 2–6 iteratively until convergence: The iterations allow for refinement of the estimated image by iteratively adjusting the pixel or voxel values based on the observed and modeled data.

2.3.2 Image denoising method

The imaging principle of the time-encoded imager was introduced in the previous section. In this study, the DOI detector was divided into N units according to position resolution, and the count vector measured by each unit was independently used for image reconstruction. Subsequently, N original images were obtained through image reconstruction.

$$\begin{cases} C_1 + \delta C_1 = (S + \delta S_1) \odot (R_1 + \delta R_1) \\ C_2 + \delta C_2 = (S + \delta S_2) \odot (R_2 + \delta R_2) \\ \qquad\qquad ...\,... \\ C_n + \delta C_n = (S + \delta S_n) \odot (R_n + \delta R_n) \\ \qquad\qquad ...\,... \\ C_N + \delta C_N = (S + \delta S_N) \odot (R_N + \delta R_N) \end{cases} \qquad Eq.\,9$$

where $C + \delta C_n$ is the measured count vector of the n-th detector unit; $R + \delta R_n$ is the simulated response matrix of the n-th detector unit; δC_n is the count error vector in the n-th detector unit, which is contributed by statistical fluctuations, background counts, and the interaction position miscue. δR_n is the response error matrix for the response matrix of the n-th detector unit. In actual measurements, the distance, type of radioactive source, and shielding around the source are unknown. That is, the emitted energy spectrum of the source to be detected is known. Therefore, the measured response differs from the simulation. An adaptive response correction method [13] was introduced in the image reconstruction process to reduce δR_n. δC_n and δR_n are reflected in the noise in the reconstructed image δS_n. S is the actual source distribution. $S + \delta S_n$ is the reconstructed image of the n-th detector unit.

A multi-detector denoising method is proposed for image denoising. This method leverages the redundancy and diversity of the information captured by multiple detectors to enhance the signal-to-noise ratio (SNR) and improve the overall output quality. This is particularly useful when dealing with low-SNR scenarios, where a single detector might not provide sufficient quality, or when the noise characteristics vary across detectors, allowing for better noise estimation and removal. The N original reconstructed images were used in the image denoising process.

$$S' = \sqrt[N]{\prod_1^N (S + \delta S_n)} \qquad Eq.\,10$$

where S' is the filtered source distribution image. Considering the source of δC_n, the noise (error) δS_n is randomly distributed on S. In different original images, noise is distributed among different pixels. Therefore, the multi-detector denoising method can effectively suppress random noise.

3 Results and Discussion

3.1 Detector calibration

In this study, information including the interaction position, interaction time, and particle type (neutron/gamma ray) of the incident particle must be obtained by the central DOI detector. Therefore, calibration experiments for the DOI detector were conducted prior to the imaging tests. Details of the calibration experiments are provided in [43].
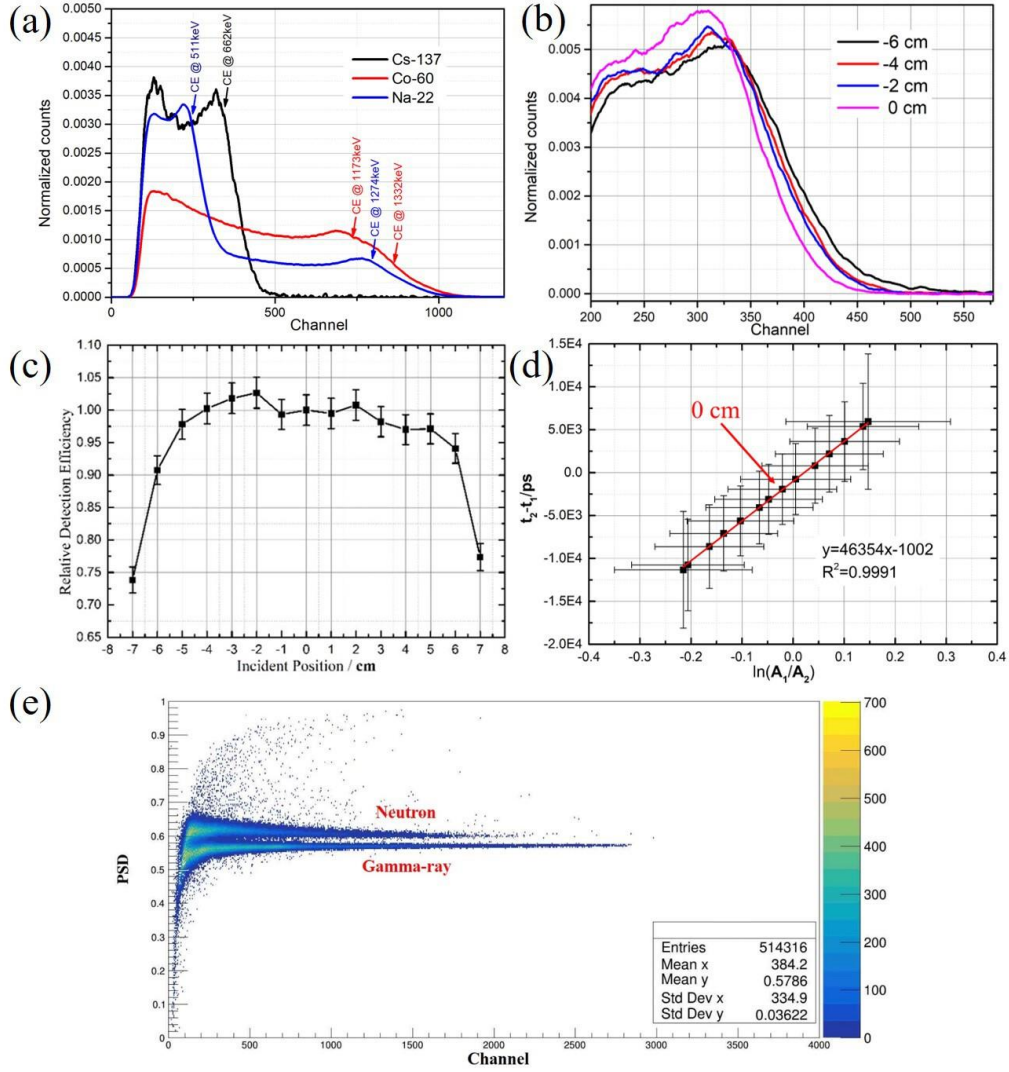
Figure 3 Energy calibration (a) with different energies (incident position at the central part), (b) with different incident positions (Cs-137), and (c) relative efficiency calibration; (d) relationship between the amplitude ratio and time difference; (e) pulse shape parameter vs. pulse amplitude.

3.1.1 Energy and relative efficiency calibration

During the measurement, a coincidence event at both ends was considered the true count. In the response function simulation, the energy threshold for gamma rays and neutrons was set to 0.2 and 0.5 MeV, respectively; the detection efficiency at different incident positions was considered to be identical. However, the detection efficiency at different incident positions differed because of different attenuation lengths. Therefore, energy and relative efficiency calibration of the DOI detector was required.

A collimated Cs-137 gamma-ray source was incident at different positions on the detector for energy (with different incident positions), relative efficiency, and position response calibration. In addition, the Cs-137, Co-60, and Na-22 gamma-ray sources were incident at the center of the detector for energy (with different energies) calibration. Energy spectra with different gamma-ray energies from different radioactive sources are shown in Figure 3(a). The Compton edges of the gamma rays for each energy level are marked. The energy spectra of Cs-137 at different incident

positions are shown in Figure 3(b).

The total counts when the Cs-137 gamma ray was incident at different positions minus the background counts were used to calibrate the relative efficiency. The relative efficiency of the detector center was considered to be 100%. As shown in Figure 3(c), for most of the central area of the detector, the relative efficiency is uniform and greater than 95%. After imager measurement, the relative efficiency was used to correct the measured counts.

3.1.2 Position response calibration

The relationship between the interaction location z and the difference in time/log of the signal amplitude ratio was determined via position-response calibration.

The hotspot moves as the incident position changes. The error bars represent the sigma value of the 2D Gaussian distribution. The time difference was larger than that of the theoretical calculations because of the timing error of the signals. The relationship between the difference in time T (ps) and log of the signal amplitude ratio A was obtained using the fitted line in Figure 3(d).

$$T = 46354 \times A - 1002 \qquad Eq.11$$

where $A = \ln(A_1/A_2)$, $T = t_1 - t_2$. The values (A and T) of each coincidence event were obtained by projecting them onto a fitted line. z can be determined using either A or T as follows:

$$z = -\frac{A + 0.0179}{0.0292} \qquad Eq.12$$

$$z = -\frac{T + 1880}{1332} \qquad Eq.13$$

Although the difference between the two results is small, their average is considered as the final result.

$$z = -\frac{\left[\left(\frac{A + 0.0179}{0.0292}\right) + \left(\frac{T + 1880}{1332}\right)\right]}{2} \qquad Eq.14$$

The interaction position of the particles at different incident positions were determined using the aforementioned method. The full width at half maximum (FWHM) of the Gauss fitting curve was considered as the position resolution. The position resolutions in the middle and two end sections of the DOI detector were approximately 4.4 and 4.9 cm, respectively. The position resolution of the middle part was slightly better than that of the edge.

3.1.3 Neutron/gamma-ray discrimination

A 1.11E10 Bq Am-Be neutron source was used for the neutron/gamma-ray discrimination experiment. Many gamma rays also exist in front of the collimator of the neutron source setup, including associated and secondary gamma rays [44]. The DOI detector was placed in a neutron/gamma-ray mixed field, and the measurement time was set to 1000 s. According to the PSD-energy value of the signal, neutron and gamma ray events were classified using a tail-to-total method [45, 46]. The times of the long (total) and short gates (total-tail) were optimized to 2800 and 500 ns, respectively. The PSD-channel distributions of the signals from the two ends were relatively consistent, as shown in Figure 3(e).

Neutron/gamma-ray discrimination is the first step in signal post-processing. For a coincidence event, the PSD-energy information was first used to determine the type of particle. If the particle type is different, this is not a true coincidence. Then, the T-A information was used to determine the interaction position. Thus, the time, particle type, and interaction position of a coincidence event can be obtained.

3.2 Influence of the detector unit length

The aforementioned mentioned Am-Be neutron source was used to verify the denoising effect and optimize the detector unit length. The source was positioned at approximately (269°, 2°) (±0.5°) in the given frame of reference. This indicates the angular coordinates of the source, with the first and second numbers representing the horizontal and vertical angles, respectively. The ±0.5° uncertainty indicates the possible range of deviations from the specified coordinates. The source-detector distance was 1.8 m. The total measurement time and rotational speed were set to 2000 s and 200 s/revolution, respectively. After each revolution, the count of each basic detector unit at different rotation angles was obtained. In the image reconstruction, the detector unit length was set to 1, 3, 5, 7, and 9 cm, respectively. In other words, the detector was divided into 15, 5, 3, 2, and 2 parts, corresponding to different detector lengths. When the detector unit length was set to 9 cm, the two detector unit parts overlap. The longer the detector unit, the smaller the error contributed by the statistical fluctuations and position miscues, but the worse the position response function, and vice versa.
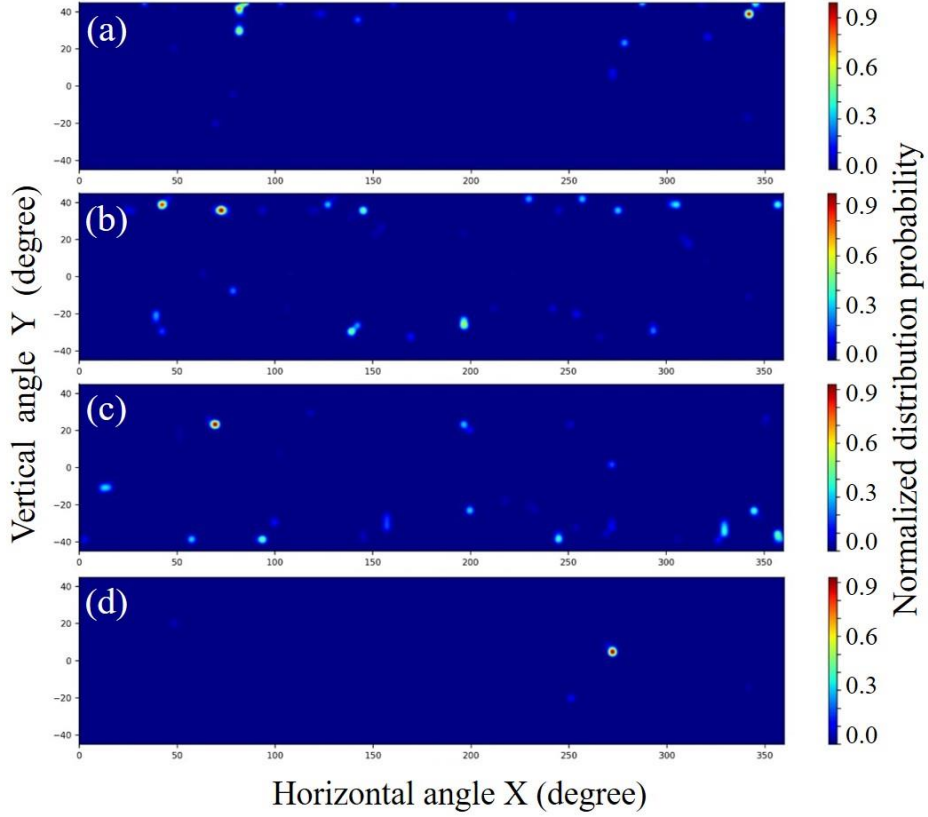

Figure 4 Original images (a–c) when the detector unit length is set to 5 cm and (d) filtered image.

First, to verify the denoising effect when the detector unit length was set to 5 cm, the original and corresponding filtered images are shown in Figure 4. There is considerable noise in the original images. As mentioned previously, the noise of each image varies. The filtered image is calculated according to Eq. 10, and random noise is effectively suppressed. However, it must also be noted that some of the events collected by the detector were considered noise owing to position miscues. This renders the imager less efficient. In other words, the better the position resolution of

the DOI detector, the better the performance of the time-encoded imager.

Theoretically, the shorter the detector length, the shaper the position response function and the greater the position miscue. The reconstructed source distribution images with different detector unit lengths were analyzed. When the detector unit length was less than 7 cm, the neutron source could be correctly located at a very low noise level. When the detector unit length was set to 1 cm (much shorter than the position resolution), the filtered images exhibited an excellent denoising effect. Finally, when the detector unit length was set to 9 cm, the filtered image exhibited relatively obvious noise.
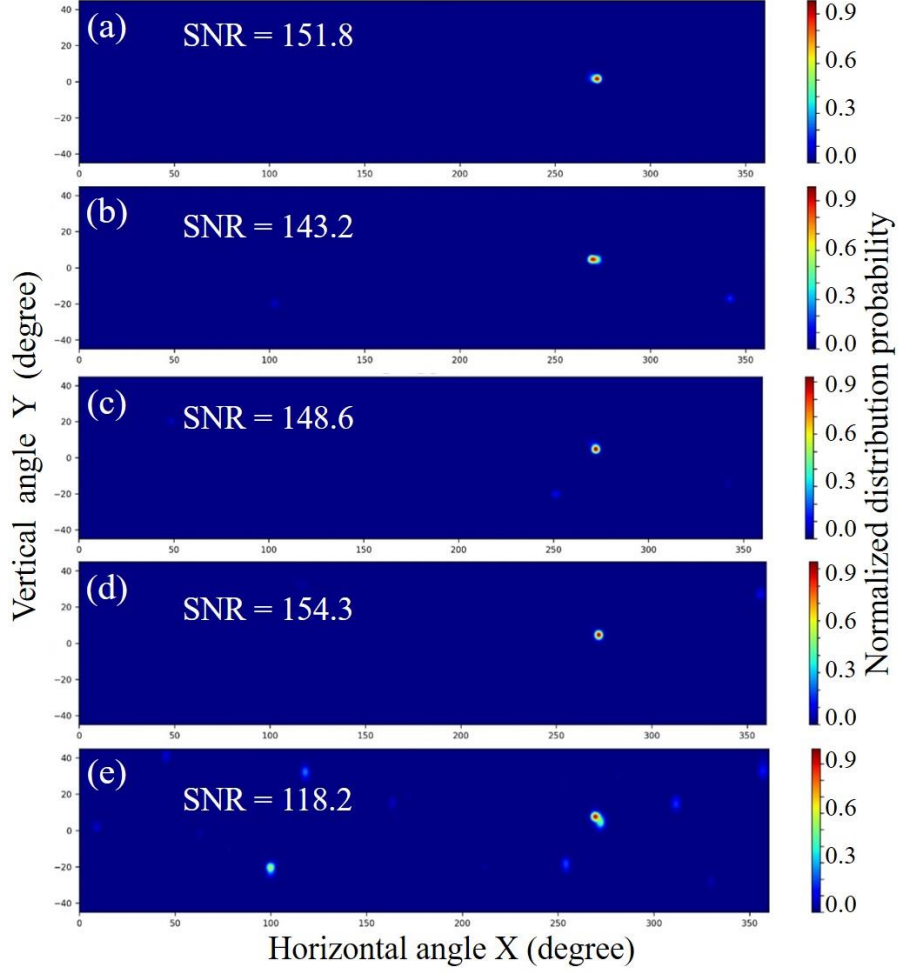

Figure 5 Reconstructed source distribution with different detector unit lengths: (a) 1; (b) 3; (c) 5; (d) 7; and (e) 9 cm.

3.3 Field-of-view verification

The FOV can be described in two ways:

(1) Angular FOV: This measurement describes the extent of the scene in terms of angle. It is typically measured in degrees, radians or arcs.

(2) Spatial FOV: This measurement quantifies the extent of the scene in terms of physical dimensions such as width and height.

For far-field imaging, angular FOV is commonly used to evaluate the performance of time-encoded imagers. For the cylindrical coded mask design, the horizontal (mask rotation direction)

angular FOV can reach 0°~360° (2π). The theoretical maximum vertical angular FOV is -90°~90°. The horizontal direction in which the center of the detector is located is considered to be 0°. The actual achievable vertical FOV is influenced by the mask height and the relative position between the detector and the coded mask.
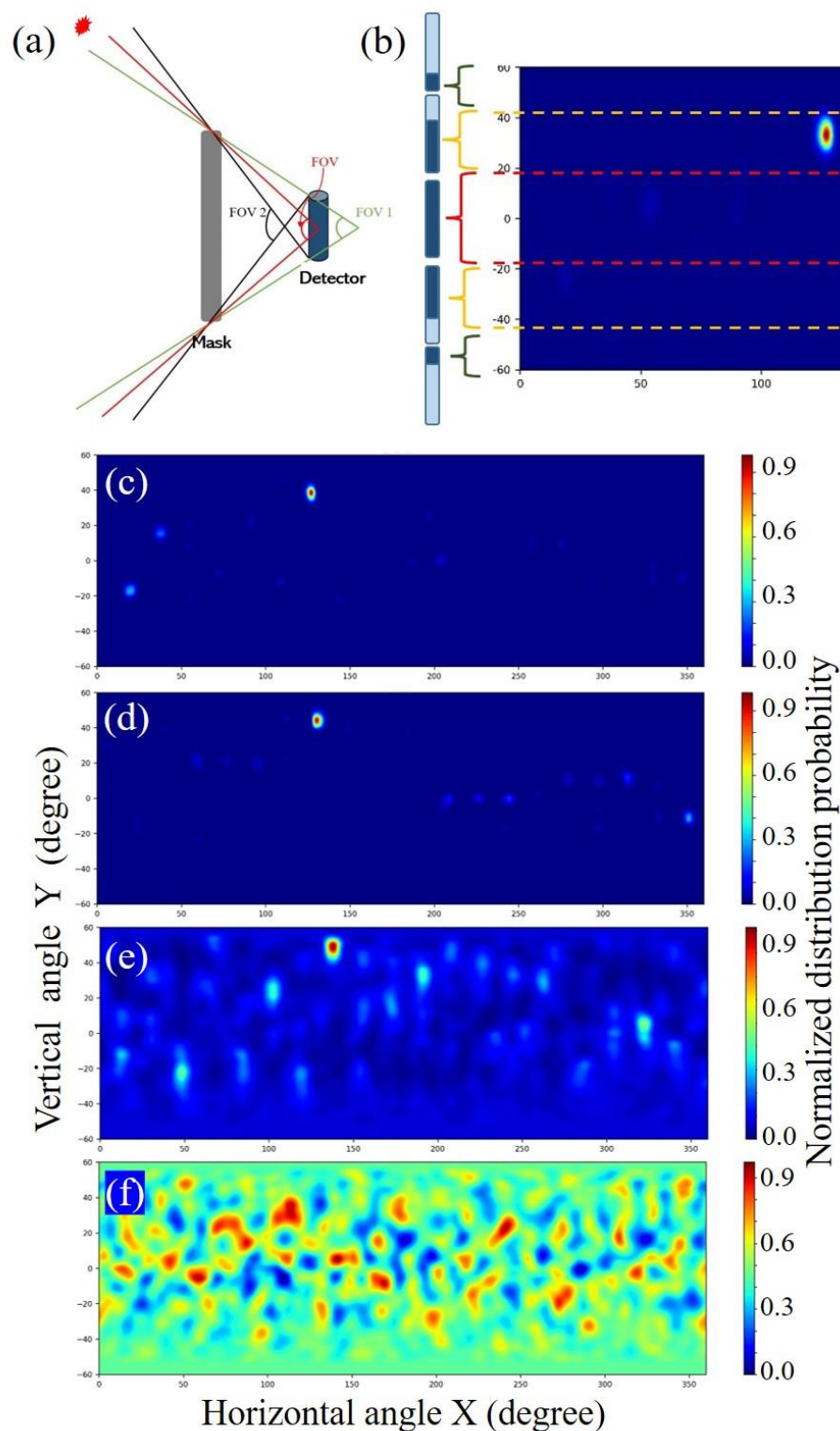

Figure 6 (a) Field-of-view schematic and (b) corresponding detector part. Reconstructed source distribution with different source position vertical angles: (c) 40°; (d) 50°; (e) 55°; and (f) 60°.

Particles from an area outside the FOV can reach the detector without passing through the mask. Therefore, the FOV differs at different detector positions. Generally, as shown in Figure 6(a), for a time-encoded imager, the FOV is considered the field of view. However, the FOV can be further extended to the DOI detector. The particles from FOV1 can reach the entire detector by passing through the mask. The particles from FOV2 can reach part of the detector by passing through the mask. The particles from outside FOV2 reach the detector without passing through the mask. Correspondingly, in image reconstruction, the total detector count can be used for FOV1, whereas for the edge area, only the count of the part detector can be used, as shown in Figure 6(b). The final large FOV image can be merged using different parts of the detector result.

A 9E5 Bq Na-22 gamma-ray source was placed at different positions (vertical angles) for the FOV verification experiments. The source-detector distance remained constant at 0.6 m. The Na-22 gamma-ray source was placed sequentially at vertical angles of 0°, 10°, 30°, 40°, 45°, 50°, 55°, and 60°. Similarly, the total measurement time and rotational speed were set to 2000 s and 200 s/revolution, respectively. The detector unit length for the image reconstruction was 3 cm.

The results for all positions are not shown here. Except for the 60° position, the source placed at any position in this experiment could be located using this imager. The results for 40°, 50°, 55°, and 60° are shown in Figure 6(c–f), respectively. It can be concluded that the vertical FOV of this imager is approximately (-55°, 55°) when the detector is placed at the center of the mask according to the reconstructed images. As shown in Figure 6(e), noise cannot be ignored. For the edge area, only one detector unit can be used for image reconstruction, and the previously mentioned denoising method cannot be used. This time-encoded imager provides better measurement on the middle part of the FOV.

3.4 20-m standoff detection

A DT neutron source [47, 48] (80 kV, 70 µA) shielded by 12 cm of lead and polyethylene with a 20-m standoff was measured to verify the sensitivity of the imager. The source was placed at (160°, -2°) (±0.5°). The neutron emission rate of the DT neutron generator was approximately 3.2E7 n/s. The total measurement time and rotational speed were set to 10000 s and 200 s/revolution, respectively. After each revolution, the count of each basic detector unit at different rotation angles was obtained to reconstruct the source distribution until the source was correctly located. The detector unit length in the image reconstruction was 3 cm.
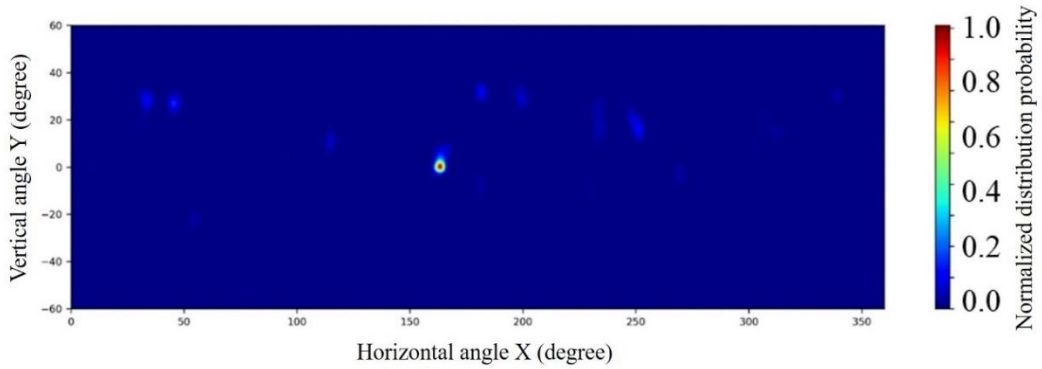

Figure 7 Reconstructed neutron source distribution after 2400 s of measurement (approximately 2800 total neutron counts).

After 2400 s of measurement (approximately 2800 total neutron counts), the DT neutron source was located. The corresponding source distribution image is shown in Figure 7, and the angular resolution (FWHM of the hotspot) was better than 3.5°. Although the neutron-induced prompt gamma rays were emitted from the surroundings of the neutron source, the detector's gamma-ray count rate was 1/7 higher than that of the background, and the gamma-ray source hotspot imaging failed. Because the neutron background count rate is much lower than that of gamma rays, for neutron and gamma-ray sources with the same emission rate, the sensitivity of the imager to neutrons is much higher than that to gamma rays.

4 Conclusions and outlooks

A time-encoded imager was designed and calibrated based on a DOI detector. The energy, relative efficiency, neutron/gamma-ray discrimination, and position resolution of the DOI detector were calibrated. An image-denoising method was proposed for the DOI-detector-based time-encoded imager to effectively suppress random noise. The horizontal FOV of the imager was 2π, while the vertical FOV was approximately (-55°, 55°). A DT neutron source shielded by 12 cm of lead and polyethylene at a 20-m standoff could be located within 2400 s with an angular resolution of 3.5°.

The better the position resolution of the DOI detector, the better the performance of the time-encoded imager. In future work, the position resolution of the DOI detector will be optimized by replacing the fast-output SiPM and adding a light guide between the scintillator and SiPM. In addition, the vertical FOV can be adjusted by changing the position of the central detector according to the measurement requirements and specific situation considered.

Author contributions

All authors contributed to the study conception and design. Material preparation, data collection and analysis were performed by Dong Zhao, Xu-Wen Liang, Ping-Kun Cai and Wei Cheng. The first draft of the manuscript was written by Dong Zhao and all authors commented on previous versions of the manuscript. All authors read and approved the final manuscript.

Data Availability Statement

The data that support the findings of this study are openly available in Science Data Bank at https://cstr.cn/31253.11.sciencedb.j00186.00123 and https://doi.org/10.57760/sciencedb.j00186.00123.

References

[1] H. Al Hamrashdi, S.D. Monk, D. Cheneler, Passive gamma-ray and neutron imaging systems for national security and nuclear non-proliferation in controlled and uncontrolled detection areas: Review of past and current status. Sensors **19**, 2638 (2019). https://doi.org/10.3390/s19112638

[2] H.Y. Lan, T. Song, J.L. Zhang et al., Rapid interrogation of special nuclear materials by combining scattering and transmission nuclear resonance fluorescence spectroscopy. Nucl. Sci. Tech. **32**, 84 (2021). https://doi.org/10.1007/s41365-021-00914-x

[3] J.S. Beaumont, M.P. Mellor, M. Villa et al., High-intensity power-resolved radiation imaging of an operational nuclear reactor. Nat. Commun. **6**, 8592 (2015). https://doi.org/10.1038/ncomms9592

[4] J.S. Beaumont, B.A. Shippen, M.P. Mellor et al., Imaging of fast neutrons and gamma rays from ^{252}Cf in a heavily shielded environment. Nucl. Instrum. Meth. A **847**, 77-85 (2017). https://doi.org/10.1016/j.nima.2016.11.043

[5] Y.W. Hou, Y.S. Song, L.Y. Hu et al., A neutron scatter imaging technique with distance determining capability. Nucl. Instrum. Meth. A **1022**, 165975 (2022). https://doi.org/10.1016/j.nima.2021.165975

[6] M.F. Yan, H.S. Hu, G. Hu et al., Comparison of heuristic and deterministic algorithms in neutron coded imaging reconstruction. Nucl. Instrum. Meth. A **985**, 164704 (2021). https://doi.org/10.1016/j.nima.2020.164704

[7] Q.K. Li, Y.D. Yan, F. Wang et al., Combination algorithms applied to source reconstruction for neutron coded images and restoration for incomplete coded images. Rev. Sci. Instrum. **94**, 053301 (2023). https://doi.org/10.1063/5.0138742

[8] E. Aboud, S. Ahn, G.V. Rogachev et al., Modular next generation fast-neutron detector for portal monitoring. Nucl. Sci. Tech. **33**, 13 (2022). https://doi.org/10.1007/s41365-022-00990-7

[9] Z.Y. Yao, Y.S. Xiao, J.Z. Zhao, Dose reconstruction with Compton camera during proton therapy via subset-driven origin ensemble and double evolutionary algorithm. Nucl. Sci. Tech. **34**, 59 (2023). https://doi.org/10.1007/s41365-023-01207-1

[10] R.C. Runkle, A. Bernstein, P.E. Vanier, Securing special nuclear material: Recent advances in neutron detection and their role in nonproliferation. J Appl. Phys. **108**, 13 (2010). https://doi.org/10.1063/1.3503495

[11] H.Y. Zhang, B. Zhong, H.Y. Shen et al., Research on a Monte Carlo Simulation Method of Neutron Coded-Aperture Imaging. Nucl. Sci. Eng. **196**, 1236-1246 (2022). https://doi.org/10.1080/00295639.2022.2070386

[12] R.J. Olesen, J.B. Cole, D.E. Holland et al., Regenerative neural network for rotating scatter mask radiation imaging. Radiat. Meas. **143**, 106565 (2021). https://doi.org/10.1016/j.radmeas.2021.106565

[13] D. Zhao, W.B. Jia, D.Q. Hei et al., Optimization of image reconstruction method for dual-particle time-encode imager through adaptive response correction. Nucl. Eng. Technol. **55**, 1587-1592 (2023). https://doi.org/10.1016/j.net.2023.02.003

[14] A. Glick, E. Brubaker, B. Cabrera-Palmer et al., Deployment of a double scatter system for directional detection of background neutron radiation. Nucl. Instrum. Meth. A **992**, 165029 (2021). https://doi.org/10.1016/j.nima.2021.165029

[15] A. Poitrasson-Rivière, M.C. Hamel, J.K. Polack et al., Dual-particle imaging system based on simultaneous detection of photon and neutron collision events, Nucl. Instrum. Meth. A **760**, 40-45 (2014). https://doi.org/10.1016/j.nima.2014.05.056

[16] X.P. Zhang, M. Zhang, L. Sheng et al., Image reconstruction of a neutron scatter camera. Sci. China Technol. Sci. **59**, 149–155 (2016). https://doi.org/10.1007/s11431-015-5922-0

[17] X.Y. Pang, Z.M. Zhang, J.P. Zhang et al., A compact MPPC-based camera for omnidirectional (4π) fast-neutron imaging based on double neutron–proton elastic scattering. Nucl. Instrum. Meth. A **944**, 162471 (2019). https://doi.org/10.1016/j.nima.2019.162471

[18] J. Boo, M.D. Hammig, M. Jeong, Compact lightweight imager of both gamma rays and neutrons based on a pixelated stilbene scintillator coupled to a silicon photomultiplier array. Sci. Rep. **11**, 15740 (2021). https://doi.org/10.1038/s41598-021-83530-4

[19] S.F. Sun, Y. Liu, X.P. Ouyang, Design and performance evaluation of a coded aperture imaging system for real-time prompt gamma-ray monitoring during proton therapy. Radiat. Phys. Chem. **174**, 108891 (2020). https://doi.org/10.1063/1.4996193

[20] M. Grodzicka-Kobylka, T. Szczesniak, M. Moszyński et al., Fast neutron and gamma ray pulse shape discrimination in EJ-276 and EJ-276G plastic scintillators. J Instrum. **15**, P03030 (2020). https://doi.org/10.1088/1748-0221/15/03/P03030

[21] P. Hausladen, M.A. Blackston, E. Brubaker et al., Fast-neutron coded-aperture imaging of special nuclear material configurations, *53rd INMM Annual Meeting*, (Orlando, Florida, USA, 15-20, Jul. 2012). https://www.osti.gov/biblio/1055983

[22] J. Guo, X.Y. Pang, J.L. Cai et al., Compact MPPC-based coded aperture imaging camera for dual-particle detection. Radiat. Detect. Technol. Meth. **5**, 61-70 (2021). https://doi.org/10.1007/s41605-020-00218-5

[23] R.S. Woolf, B.F. Phlips, A.L. Hutcheson et al., Fast-neutron, coded-aperture imager. Nucl. Instrum. Meth. A **784**, 398-404 (2015). https://doi.org/10.1016/j.nima.2015.01.084

[24] J. Brennan, E. Brubaker, M. Gerling et al., Source detection at 100 meter standoff with a time-encoded imaging system. Nucl. Instrum. Meth. A **877**, 375-383 (2018). https://doi.org/10.1016/j.nima.2017.09.052

[25] D.M. Wang, I.N. Ruskov, H.S. Hu et al. Gamma-ray imaging with a time-modulated random coded aperture. Rev. Sci. Instrum. **90**, 015107 (2019). https://doi.org/10.1063/1.5050211

[26] J. Brennan, E. Brubaker, M. Gerling et al., Demonstration of two-dimensional time-encoded imaging of fast neutrons. Nucl. Instrum. Meth. A **802**, 76-81 (2015). https://doi.org/10.1016/j.nima.2015.08.076

[27] Z. Zhou, S.G. Li, Q.S. Tan et al., Optimization method of Hadamard coding plate in γ-ray computational ghost imaging. Nucl. Sci. Tech. **34**, 13 (2023). https://doi.org/10.1007/s41365-022-01164-1

[28] X.Z. Liang, X.Y. Pang, D.Q. Cao et al., Self-supporting design of a time-encoded aperture, gamma-neutron imaging system. Nucl. Instrum. Meth. A **951**, 162964 (2020). https://doi.org/10.1016/j.nima.2019.162964

[29] N. Shah, Dissertation (Adaptive Imaging with a Cylindrical, Time-Encoded Imaging System, UNIVERSITY OF MICHIGAN, 2020)

[30] H.S. Kim, J. Lee, S. Choi et al., Design and fabrication of CLYC-based rotational modulation collimator (RMC) system for gamma-Ray/Neutron dual-particle imager. J. Radiat. Prot. Res. **46**, 112-119 (2021). https://doi.org/10.14407/jrpr.2021.00262

[31] A. Barzilov, A. Guckes, Time encoded imaging of neutrons and photons using CLYC detector equipped with a dual mode collimator. Sensors & Transducers **229**, 78-83 (2019). https://sensorsportal.com/HTML/DIGEST/january_2019/Vol_229/P_3060

[32] B.R. Kowash, D.K. Wehe, A unified near-and far-field imaging model for rotating modulation collimators. Nucl. Instrum. Meth. A **637**, 178-184 (2011). https://doi.org/10.1016/j.nima.2010.12.037

[33] P. Marleau, J. Brennan, E. Brubaker et al., Time encoded fast neutron/gamma imager for large standoff SNM detection, *2011 IEEE Nuclear Science Symposium Conference Record* (Valencia, Spain, 23-29 Oct. 2011),. https://doi.org/10.1109/NSSMIC.2011.6154118

[34] A. Poitrasson-Rivière, J.K. Polack, M.C. Hamel et al., Angular-resolution and material-characterization measurements for a dual-particle imaging system with mixed-oxide fuel. Nucl. Instrum. Meth. A **797**, 278-284 (2015). https://doi.org/10.1016/j.nima.2015.06.045

[35] N.P. Shah, P. Marleau, J.A. Fessler et al., Improved Localization Precision and Angular Resolution of a Cylindrical, Time-Encoded Imaging System From Adaptive Detector Movements. IEEE Trans. Nucl. Sci. **68**, 410-425 (2021). https://doi.org/ 10.1109/TNS.2021.3060071

[36] N.P. Shah, J. VanderZanden, D.K. Wehe, Design and construction of a 1-D, cylindrical, dual-particle, time-encoded imaging system. Nucl. Instrum. Meth. A **954**, 161785 (2020). https://doi.org/10.1016/j.nima.2019.01.012

[37] J.W. Du, X.W. Bai, S.R. Cherry, A depth-of-interaction encoding PET detector module with dual-ended readout using large-area silicon photomultiplier arrays. Phys. Med. Biol. **63**, 245019 (2018). https://doi.org/10.1088/1361-6560/aaee32

[38] N.P. Giha, W.M. Steinberger, L.Q. Nguyen et al., Organic glass scintillator bars with dual-ended readout. Nucl. Instrum. Meth. A **1014**, 165676 (2021). https://doi.org/10.1016/j.nima.2021.165676

[39] M. Ito, S.J. Hong, J.S. Lee, Positron emission tomography (PET) detectors with depth-of-interaction (DOI) capability. Biomed. Eng. Lett. **1**, 70-81 (2011). https://doi.org/10.1007/s13534-011-0019-6

[40] E.V. Ryabeva, I.V. Urupa, E.E. Lupar et al., Calibration of EJ-276 plastic scintillator for neutron–gamma pulse shape discrimination experiments. Nucl. Instrum. Meth. A **1010**, 165495 (2021). https://doi.org/10.1016/j.nima.2021.165495

[41] D. Zhao, W.B. Jia, D.Q. Hei et al, Influence of coded mask rotation speed and central detector to imaging performance for time-encoded imager. Radiat. Phys. Chem. **209**, 110964 (2023). https://doi.org/10.1016/j.radphyschem.2023.110964

[42] R.J. Olesen, D.E. Holland, E.M. Brubaker et al., Maximum likelihood reconstructions for rotating scatter mask imaging. Radiat. Meas. **137**, 106441 (2020). https://doi.org/10.1016/j.radmeas.2020.106441

[43] D. Zhao, X. Liang, R. Zhang et al., Design and calibration of depth of interaction detector for neutrons and gamma-rays (In Chinese). Nucl. Tech. **46**, 070402 (2023). https://doi.org/10.11889/j.0253-3219.2023.hjs.46.070402

[44] D. Zhao, W.B. Jia, D.Q. Hei et al., Design of a neutron shielding performance test system base on am–be neutron source. Radiat. Phys. Chem. **193**, 109954 (2022). https://doi.org/10.1016/j.radphyschem.2021.109954

[45] A. Jančář, Z. Kopecký, J. Dressler et al., Pulse-shape discrimination of the new plastic scintillators in neutron–gamma mixed field using fast digitizer card. Radiat. Phys. Chem. **116**, 60-64 (2015). https://doi.org/10.1016/j.radphyschem.2015.05.007

[46] C. Liao, H.R. Yang, Pulse shape discrimination using EJ-299-33 plastic scintillator coupled with a Silicon Photomultiplier array. Nucl. Instrum. Meth. A **789**, 150-157 (2015). https://doi.org/10.1016/j.nima.2015.04.016

[47] H.Y. Lei, W.B. Jia, D.Q. Hei et al. Dose rate evaluation in a laboratory for prompt gamma neutron activation analysis by Monte Carlo simulation. J. Radioanal. Nucl. Chem. **327**, 477–483 (2021). https://doi.org/10.1007/s10967-020-07510-0

[48] C. Cheng, Y.J. Xie, X.R. Xia et al. Neutron collimator optimization for 14.1 MeV DT neutrons using Monte Carlo and Genetic algorithms. Appl. Radiat. Isot. **198**, 110838 (2023). https://doi.org/10.1016/j.apradiso.2023.110838